


Combined Purification and Crystal Growth of CsPbBr₃ by Modified Zone Refining

Published as part of the Virtual Special Issue "Mercuri G. Kanatzidis at 65"

Yu Wu¹, Matthew F. Webster¹, Brian Joy², Steve Beyer², David Kunar¹, Ramjee Kandel¹, Matthew Leybourne², Alexandre Voinot², and Peng Li Wang^{1*} 

¹ Department of Chemistry, Queen's University, 90 Bader Ln, Kingston, ON K7L 2S8, Canada

² Department of Geological Sciences and Geological Engineering, Queen's University, 36 Union St, Kingston, ON K7L 2N8, Canada

* Corresponding author, E-mail: wang.peng@queensu.ca

Abstract

The all-inorganic semiconducting perovskite Cesium Lead Bromide, CsPbBr₃, exhibits promising properties for ionizing radiation detection applications. In this work, polycrystalline CsPbBr₃ was synthesized from the melt of binary compounds CsBr and PbBr₂. Moisture and oxides in the synthesized CsPbBr₃ compounds were removed by a reduction process under hydrogen. The CsPbBr₃ materials were purified and grown into high-quality single crystals via a modified zone refining process. The single-crystal samples obtained from the combined zone-refining/crystal growth process exhibited total trace impurity levels below 1 ppm (w.t.). Obtained single crystals exhibited an electrical resistivity within a range of 10⁸–10⁹ Ω·cm. Stoichiometry imbalance was observed in the CsPbBr₃ crystal growth. Around 1% Cs deficiency was observed in all the samples, despite different ratios between the starting materials of PbBr₂ and CsBr. The positive impact of excess PbBr₂ in starting materials was also revealed. With a slight excess Pb (2%), CsPbBr₃ single crystals displayed significantly higher photosensitivity compared to the stoichiometric or excess Cs samples.

Key words: Opto-electronic Material; Radiation detector; Perovskites; Compound Semiconductor

Citation: Yu Wu, Matthew F. Webster, Brian Joy, Steve Beyer, David Kunar, et al. Combined Purification and Crystal Growth of CsPbBr₃ by Modified Zone Refining. *Materials Lab* 2022, 1, 220019. DOI: [10.54227/mlab.20220019](https://doi.org/10.54227/mlab.20220019)

1 Introduction

Room-temperature semiconducting ionizing radiation detectors have been applied in many different fields, such as medical imaging, national security, and scientific research.^[1–3] Effective semiconductor radiation detectors must satisfy a number of requirements, including a high density and high effective atomic number, to achieve a high radiation stopping power, as well as a large bandgap and high resistivity to suppress the thermal excitation of charge carriers.^[4] To achieve high charge collection efficiency during the radiation detection process, the mobility-lifetime product ($\mu\tau$) of the detector material plays an important role. A higher $\mu\tau$ guarantees a longer mean drift length (λ) under a given electric field, leading to an effective collection of photo-generated charges.^[5]

Researchers have investigated and developed several high-performance compound semiconductor detectors such as cadmium zinc telluride (CZT) and Thallium bromide (TlBr).^[6–8] However, the commercial benchmark material, CZT, still suffers from a high concentration of Te inclusions/precipitates, uneven distribution of Cd and Te, and high production cost.^[7,9–11] TlBr detectors suffer from chemical instability and low hardness.^[5,12,13] Therefore, it is important to explore alternative

high-performance radiation detection materials suitable for low-cost, high-volume production.

The lead halide perovskites have received significant research attention for the past decade because of their excellent optoelectronic properties, such as high carrier mobility and long diffusion length. So far, these halides have been widely used in photodetectors, solar cells, as well as high-energy radiation detectors.^[6,14–19] Compared to the organic-inorganic hybrid perovskites, the all-inorganic perovskites show excellent mechanical stability, making them suitable for a broader range of applications.^[20–22] As a prominent member of the inorganic halide perovskite family, cesium lead bromide (CsPbBr₃), was first investigated as a radiation detector in 2013 by Stoumpos *et al.*^[23] High-quality single-crystal detectors displaying excellent gamma-ray spectrometry response were prepared by He *et al.* in 2018.^[24] CsPbBr₃ possesses an effective atomic number of 65.9 (Z_{eff}), giving rise to an excellent stopping power for gamma-ray photons; a large direct bandgap of 2.25 eV to prohibit leakage current; a high defects tolerance and a low melting point for easy crystal growth development. More importantly, CsPbBr₃ shows a superior carrier mobility lifetime product for both electrons and holes, which facilitates its high radiation detection efficiency.^[23–26] Compared to its poly- or nano-crystalline

Received 31 March 2022; Accepted 3 June 2022; Published online

© 2022 The Author(s). *Materials Lab* published by Lab Academic Press

form, a bulk CsPbBr_3 single crystal exhibits consistent bulk physical properties and better photo-electrical performances, as it is free of grain boundaries and less affected by extrinsic defects.^[20,27,28] Thus, the growth of large, high-purity single crystals is crucial for the development of the CsPbBr_3 material.

Currently, the state-of-the-art CsPbBr_3 single crystals are obtained *via* multi-step processes involving separated reaction vessels and apparatuses.^[26,29–31] To achieve the high purity necessary for semiconducting detector operations,^[5] the precursor materials, PbBr_2 and CsBr , are usually purified separately and subsequently combined in a new reaction vessel for synthesis and crystal growth. Such processes place strict requirements for experimental technique and environmental control to prevent unintentional introduction action of trace impurity. In addition, the isolated purification, synthesis, and crystal growth protocols each have their thermal cycles (*i.e.*, heating/cooling time), resulting in relatively low production efficiency. Hence, there is a need to develop more efficient purification and growth protocols for the development of CsPbBr_3 based single crystal radiation detectors.

In this work, we report a modified zone-refining technique that combines the purification and the crystal growth of CsPbBr_3 into a continuous process in a single reaction vessel. A set of reliable and reproducible procedures were developed to produce high-quality CsPbBr_3 single crystals with excellent photosensitivity. The obtained CsPbBr_3 crystals

were subjected to compositional and trace element analyses to study the effect of minor stoichiometric imbalance. The optimized single crystal detectors were used to collect the pulse-height spectra of a radiation source.

2 Materials and Methods

2.1 Materials

The reagents and materials were used as acquired from commercial sources without further purification. (i) Lead (II) bromide, 99.999% (*w.t.*%, metals basis), Sigma-Aldrich; (ii) Cesium bromide, 99.999% (*w.t.*%, metals basis), Sigma-Aldrich; (iii) Methanol, Semiconductor Grade, 99.9% min, Alfa Aesar. (IV) PELCO® Conductive Silver Paint, TED PELLA. (V) Gallium metal, 99.999% (*w.t.*%, metals basis), Alfa Aesar.

2.2 Synthesis, purification, and crystal growth of CsPbBr_3

Polycrystalline CsPbBr_3 was synthesized from binary CsBr and PbBr_2 precursors in a tapered fused quartz ampoule (25 mm OD, 22 mm ID and 350 mm length). The reaction vessel containing the sample was first heated to 120 °C under a dynamic vacuum for one hour to remove moisture and then heated at 570 °C for an hour under a slow-flowing hydrogen gas stream to complete the synthesis (Fig. 1a). The synthesized sample was cooled to room temperature under hydrogen and then flame-sealed under 0.3 atm of H_2 pressure.

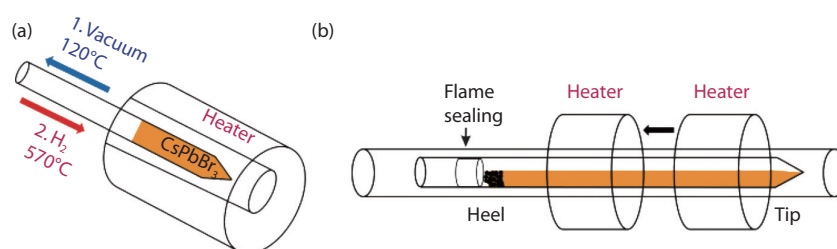


Fig. 1 System design for (a) H_2 reduction and (b) Horizontal zone refining furnace.

The sealed sample was subsequently subjected to zone-refining cycles. A tube furnace with a 4-inch heated zone was heated to a maximum temperature of 600 °C. The heater was moved along the length of the CsPbBr_3 -containing ampoule from the “tip” side to the “heel” side (Fig. 1b). The furnace movement was controlled at a speed of 10-20 mm/hour by a programmable linear motion system. Fig. 2 shows the temperature profile of a typical zone-refining cycle.

Upon completing each pass, the heater was quickly repositioned in front of the tip of the sample before the start of the next pass. After a number of zone-refining passes at a higher speed, the sample was subjected to slower passes to promote crystal growth. Table 1 shows the growth history of all samples discussed in this article. Three samples, 1127, 1149, and 1153 were grown via the zone refining method, while a baseline sample labelled 1100 was grown using the previously reported vertical Bridgman method.^[23] Different ratios of precursor materials PbBr_2 and CsBr were used to investigate the optimal molar ratio between Pb and Cs. And different zone-refining speeds were tested to improve the crystallinity.

2.3 Post-growth process

The as-grown CsPbBr_3 ingots obtained from the zone refin-

ing furnace were then sliced into 2-3 mm thick wafers by a precision saw with a 0.010 mm/s feeding rate (Struers Accutom-10). The sliced wafers were lapped and polished using an automatic Ecomet 30 polisher with SiC sandpapers of successively finer grits. The finely polished samples are approximately 1.5 mm in thickness. The roughness was measured by profilometer with 3 mg stylus force.

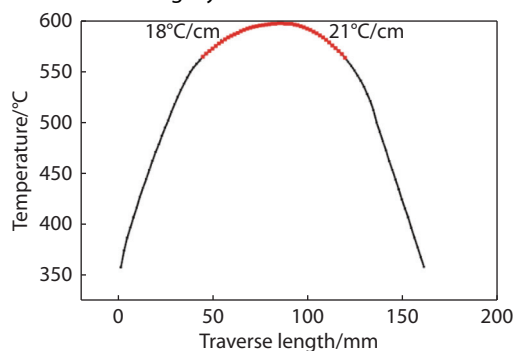


Fig. 2 Temperature profile for a typical zone-refining cycle, where the red region marks the temperature above the melting point (567 °C).

Table 1. Growth history of 4 samples.

Sample	Zone refining	Pb/Cs molar ratio	Traverse speed
1100	No	1.00: 1.00	N/A
1127	Yes	1.00: 1.00	20 mm/h X 1, 5 mm/h X 4
1149	Yes	1.02: 1.00	10 mm/h X 10, 5 mm/h X 1
1153	Yes	1.00: 1.01	10 mm/h X 2, 5 mm/h X 3

2.4 Powder X-ray diffraction (XRD)

To identify the phase purity, as-grown single crystals were subjected to XRD analysis. About 2-3 mg of sample was ground to a fine powder and evenly placed on a zero background Si sample holder. XRD data were collected by using a Bruker D2 Phaser diffractometer using Cu $K\alpha$ radiation ($\lambda = 1.5418 \text{ \AA}$) generated at a power of 30 kV \times 10 mA in the 2θ range of 10-80°, with a step size of 0.002°. The crystal grown from zone refining exhibited a pure orthorhombic phase at room temperature, referencing the calculated data.

2.5 Inductively coupled plasma mass spectrometry (ICP-MS)

Trace impurity analysis in CsPbBr₃ was performed by ICP-MS. Samples (~0.1 g of each) were dissolved with 2% HNO₃ and deionized water at 85 °C on a hotplate and then sonicated to dissolution. Samples were measured for major and trace element concentrations by Thermo Scientific iCAPTM PRO inductively coupled plasma optical emission spectrometer (ICP-OES), and iCAPTM triple quadrupole inductively coupled plasma mass spectrometry (TQ ICP-MS). AQUA1, SLRS6 and NIST1643f certified reference materials were measured at regular time intervals (n=5 samples) throughout the sequence to ensure accuracy and reproducibility of the measurements. Sample replicates were also measured to ensure the reproducibility of measurements. Calibration standards were run throughout the sequence to check and correct for any potential drift. The TQ was operated in three modes: single quadrupole with no cell gas (Li, Be, B, Sc, Ti, V, Mn, Ni, Cu, Ga, Ge, Rb, Nb, Pd, Sb, Te, Ba, Ce, Pr, Nd, Re, Tl, Bi, U), single quadrupole in KED mode (He collision gas; Na, Mg, Al, Si, K, Ca, Fe, Co, Zn, Se, Zr, Mo, Ru, Rh, Ag, Cd, Sn, La, Sm, Eu, Dy, Ho, Er, Yb, Ta, W, Os, Ir, Pt, Au, Th) and triple-quadrupole with O₂ as the reaction gas, utilizing mass shifting (P, S, Cr, As, Sr, Y, Gd, Tb, Tm, Lu, Hf).

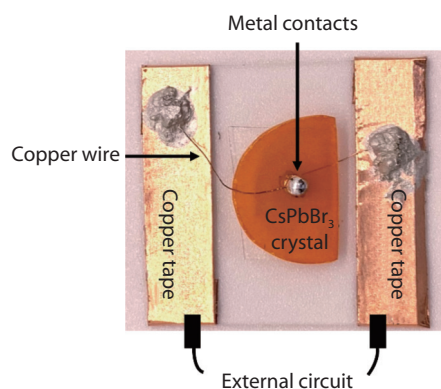
2.6 Wavelength Dispersive X-Ray Spectroscopy (WDS)

WDS was used to accurately identify the elemental composition of different CsPbBr₃ samples. The CsPbBr₃ crystals were first embedded in epoxy to form round mounts 2.5 cm in diameter. Grinding was done using a Struers LaboPol-30 lapping instrument, resin-bonded diamond grinding discs (220, 500, 1200 grit), and mineral oil coolant. The mounts were then polished using the LaboPol-30, synthetic fibre polishing cloths, diamond pastes (9, 6, 3, 0.25 μm), and oil-based coolant, followed by cleaning using methyl alcohol. Wavelength dispersive analyses were performed using a JEOL JXA-8230 electron microprobe. The accelerating potential was 15 kilovolts, and the beam current was 10 nanoamps. The beam was defocused to a diameter of 10 microns to minimize beam damage. Peak and background count times for each

X-ray line were 20 seconds each. Standards used in the analyses were synthetic CsTiOAsO₄ (Cs $L\alpha$), natural galena (Pb $M\alpha$), and synthetic eutectic TI (Br, I) (Br $L\alpha$). The raw X-ray data were processed using the PAP model of Pouchou and Pichoir in conjunction with mass absorption coefficients of Heinrich.^[32,33] Secondary fluorescence was likely insignificant, and so corrections for it were omitted. X-ray counting error was estimated using equations presented by Williams.^[34]

2.7 Photo-electrical measurements

The CsPbBr₃ detector devices were prepared by creating metal contacts on both sides of the polished crystals, shown in Fig. 3. The contacts were prepared by attaching colloidal silver paint or liquid gallium metal to the top and bottom surface of the crystal. Copper wire and tape were used to connect metal contacts to the external circuit. Similar to existing studies, the CsPbBr₃ devices were placed in a dark metal box to block ambient light.^[35] Characteristic current-voltage (I-V) curves were measured by connecting the device to a Keithley 6517b electrometer to control the external bias, and each recorded data point was an average of 10 measurements. Photosensitivity data was measured and collected over time under a constantly applied forward bias coupled with a blue LED light (20 mW) turning on and off at a set time interval inside a dark metal box. The photocurrent was recorded as a function of time.

**Fig. 3** Main components of a fabricated CsPbBr₃ test device.

2.8 Raman Spectroscopy

Black impurity powder in the heel end of the crystal bulk after zone refining was collected and analyzed by a Renishaw InVia Raman Spectrometer to reveal the chemical composition and structure information. A 633 nm wavelength laser was used to probe the molecular vibrations of the sample. The sample was analyzed at 10% power, with an exposure time of 30 s, and three accumulations for each area were analyzed. A 50 \times objective was used to focus the laser onto the surface, and the spot size analyzed was ~1 μm in diameter. Seven spots in total were analyzed.

2.9 Pulse-height spectrum measurements

The pulse height spectra of a ²⁴¹Am source were collected using a CsPbBr₃ crystal device fabricated with a Ga\CsPbBr₃\Ga contact configuration. The device was irradiated from the top in an electrically insulated dark box with a 0.9 μCi ²⁴¹Am source. The bottom Ga contact was connected

to the ground and the top contact was connected to a Cr-Z-110-HV preamplifier from Cremat. The bias voltages used for the different trials were supplied by a Keithley 6517b electrometer. The preamplifier output was connected to a Red Pitaya STEMLab running MCA software. The data for each trial was collected for 15 min and used a sampling window of 4.1 μ s.

3 Results and Discussion

3.1 Synthesis and crystal growth

The binary precursors, CsBr and PbBr₂, were mixed and heated at 120 °C in the quartz ampoule under dynamic vacuum to remove moisture. Polycrystalline CsPbBr₃ was then synthesized from the melt of the binaries under a slow-flowing hydrogen gas stream. During the synthesis, residual moisture, oxygen, and oxides in the CsPbBr₃ samples were removed by the reductive hydrogen atmosphere. This reduction process is essential to prevent the sample degradation and ampoule failure caused by oxides.

3.2 Evaporation control by H₂ gas pressure

The CsPbBr₃ materials were purified by the faster zone-refining passes, while the slower final pass promotes the formation of large single crystals. Similar approaches were employed for the preparation of high purity TlBr single crystals.^[36,37] In contrast to TlBr, CsPbBr₃ exhibits a much higher melting point leading to complex off-stoichiometry behaviours stemming from the volatility of the binary salt precursors.

In earlier experiments, the pre-synthesized CsPbBr₃ samples were sealed under a high vacuum of 1×10^{-4} mbar. During zone-refining, severe decomposition of CsPbBr₃ was observed where binaries evaporated while heating, condensed and solidified on the ampoule after cooling down (Fig. 4a). WDS was used to identify the elemental composition of the solidified vapour particles, and the results are shown in Table 2. Two phases were detected, which were identified as PbBr₂ and CsPb₂Br₅, respectively. The test data of phase 1 were normalized based on the mole fraction of Pb, and the data of phase 2 and other samples were normalized based on the mole fraction of Cs.

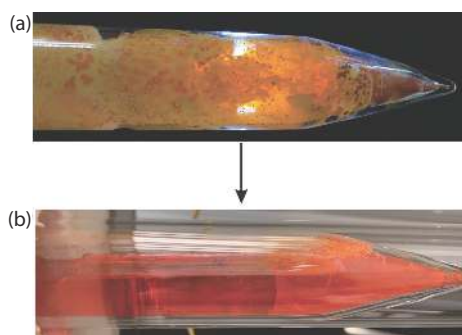


Fig. 4 Comparison of zone refining performances between two sealing techniques (a) sealing under a high vacuum, (b) sealing with 0.3 atm of H₂ gas.

To suppress the volatilization of the precursors, we implemented a H₂ gas back fill procedure, where the pre-synthesized CsPbBr₃ was flame-sealed under 0.3 atm of H₂ pressure.

The 0.3 atm pressure was used because a higher amount of H₂ would cause the flame sealing process to fail. This H₂ pressure effectively controlled the vapour pressure in the ampoule and diminished the volatilization of the binary salts during the zone refining. With a better stoichiometry control, a uniform melt along the crystal bulk was achieved with no residual unmolten chunks (Fig. 4b). A small number of solidified particles were observed after zone refining under H₂ pressure. These particles were characterized by XRD as pure CsPbBr₃.

Table 2. WDS analysis results of the vapour particles sample. *

Sample	Elemental mole fraction		
	Cs	Pb	Br
Phase 1	0.01 ± 0.02	1.00 ± 0.02	1.953 ± 0.009
Phase 2	1.000 ± 0.004	2.04 ± 0.01	5.11 ± 0.01

(*: It is worth noting that the WDS test for CsPbBr₃ samples displayed slightly low analytical totals due to systematic errors in the matrix corrections.)

3.3 Carbon impurity identification and removal

When the purification and crystal growth processes were completed, large single crystal CsPbBr₃ sections were obtained. Along the direction of furnace movement, the tip and middle parts of the samples (first to freeze) appeared to be orange in colour and highly transparent. The heel sections (last to freeze) were darker to opaque-black in colour, demonstrating a strong accumulation of black impurity to the heel end (shown in Fig. 5a and 5b). The clear sections of the as-grown samples were processed by cutting (Fig. 5c) and polishing. The processed crystals displayed good transparency (Fig. 5d).

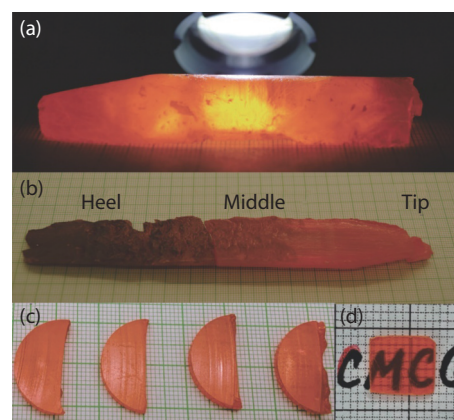


Fig. 5 (a) and (b) CsPbBr₃ bulk after zone refining. (c) As-cut crystal wafers. (d) The polished detector.

While the transparent samples were fabricated into detector or devices for photo-electrical measurements, the dark, opaque parts were subjected to impurity analysis. Black impurity often appeared after samples completed the reduction process and zone refining. During the zone refining, black impurity accumulated to last-to-freeze and segregated at the heel end of the sample. Based on the chemical behaviour of the black impurity, we suspected it mainly consists of carbon from the decomposition of organic solvent residue in the precursors.^[29]

To isolate the black impurity from CsPbBr₃ material, a vacuum sublimation of the heel pieces was performed (Fig. 6 insert). Isolated black impurity powder was collected and subjected to Raman spectroscopy analysis to identify its composition and structure. Seven spots were investigated, and the corresponding spectra were normalized to the same peak height. As Fig. 6 shows, all seven spots contain peaks at 1356 cm⁻¹ and 1580 cm⁻¹, which matches with amorphous carbon reference.

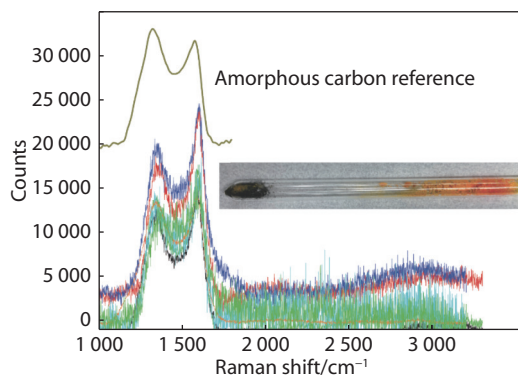


Fig. 6 Raman spectra of black impurity. Insert shows the isolation of the black impurity from CsPbBr₃ by sublimation.

3.4 Trace impurity analysis of CsPbBr₃ single crystals by Inductively coupled plasma mass spectrometry (ICP-MS)

In addition to carbon, other trace impurity elements in the CsPbBr₃ samples are also expected to segregate towards the tip or the heel during zone refining. Based on early research in our group, an ICP-MS protocol has been developed to detect trace impurity levels in CsPbBr₃ single crystals.^[38] Here, ICP-MS was used to analyze up to 66 trace elements in the CsPbBr₃ single crystals. Most trace elements exhibited a concentration level that lies below the method quantification limits in all samples. After zone refining, the total impurity concentration of most samples is below 1 ppm, indicating a high purity level of grown single crystals. The two dominating trace impurities are Na and Rh (90% of the total impurity concentration), which might be introduced from the precursor materials. Compared to sample 1100, which did not go through any zone refining, most of the samples which were purified *via* zone refining reached a lower total impurity level, indicating the efficiency of the zone refining purification process, shown in Appendix A. For sample 1149, crystal pieces from different locations along with the bulk from the tip to heel (Fig. 7 insert) were taken for ICP-MS measurements. The results are shown in Fig. 7. There is a clear trend that the total impurity level increases along the zone refining direction (*i.e.*, from the first to freeze to the last to freeze). The closer the tested pieces are to the heel part, the more impurity it contains. The concentrations of all 66 trace elements detected in the sample 1149 w030 are listed in Appendix B.

3.5 Resistivity and photoresponse tests of CsPbBr₃ semiconductor

To evaluate the properties of the CsPbBr₃ crystals, clear CsPbBr₃ wafers were lapped and polished to a maximum sur-

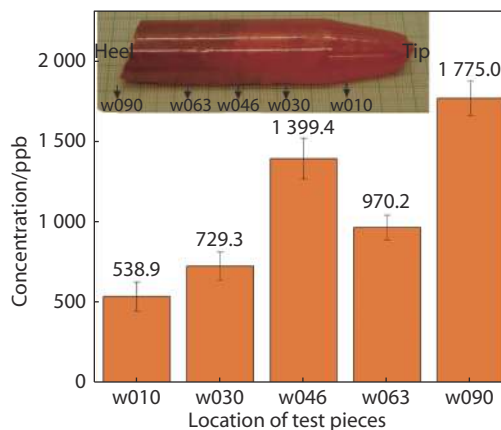


Fig. 7 Total impurity levels of samples 1149 at different positions along with the crystal bulk. Insert shows the position of testing pieces taken from sample 1149, *e.g.*, 'w010' indicates 10 mm from the tip of the bulk.

face roughness 0.1 μm. The polished wafers showed uniform change of transparency under a transmissive polarized light source, suggesting their single crystalline nature. In addition, X-ray diffraction measurements were performed on several wafers of the same ingot, which exhibited dominating preferred orientation along the (002) crystal plane. The single crystal wafers were fabricated into detector devices, which were then subjected to the current-voltage (I-V) tests and photo-response measurements. These photo-electrical data form a series of comparable feedback to guide the preparative experiments to produce single crystals with the highest signal-to-noise (SNR) ratio under the illumination of a light source.

Heel pieces containing high concentrations of carbon impurity exhibited an extremely low SNR (less than 5) because the carbon impurity could act as trapping centers for charge carriers and reduce the photosensitivity of the material. Similarly, the Bridgman-grown sample (1100), which did not undergo zone refining purification, exhibited low photosensitivity with an average signal-to-noise ratio (SNR) less than 5 at both 50 V and 100 V bias, shown in Fig. 8a. In contrast, a detector fabricated from a zone-refined sample of the same starting materials (1127, middle section) exhibited a photo-response with an SNR over 130 at 50 V. This result demonstrates the high efficiency of the zone-refining technique in terms of removing carbon-related impurities.

While all the clear, transparent CsPbBr₃ samples produced from the combined zone-refining and crystal growth method exhibited significance higher photo-electrical response, minor stoichiometry deviations in these zone-refined CsPbBr₃ samples can strongly modify their electrical behaviours. We have prepared a series of CsPbBr₃ with varying Cs: Pb ratios *via* the optimized zone-refining method, as well as *via* the Bridgman method. WDS was used to determine the elemental composition of all the as-grown CsPbBr₃ samples. Table 3 shows the Cs/Pb molar ratios of 4 samples. Despite the different growing methods and starting compositions, the molar ratios of Cs: Pb in the grown crystals are all close to 1:1.012 ± 0.007. This result elucidated a natural tendency for the CsPbBr₃ crystals to maintain a Cs deficiency. This also indicates that a slight deviation from the stoichiometry of starting materials

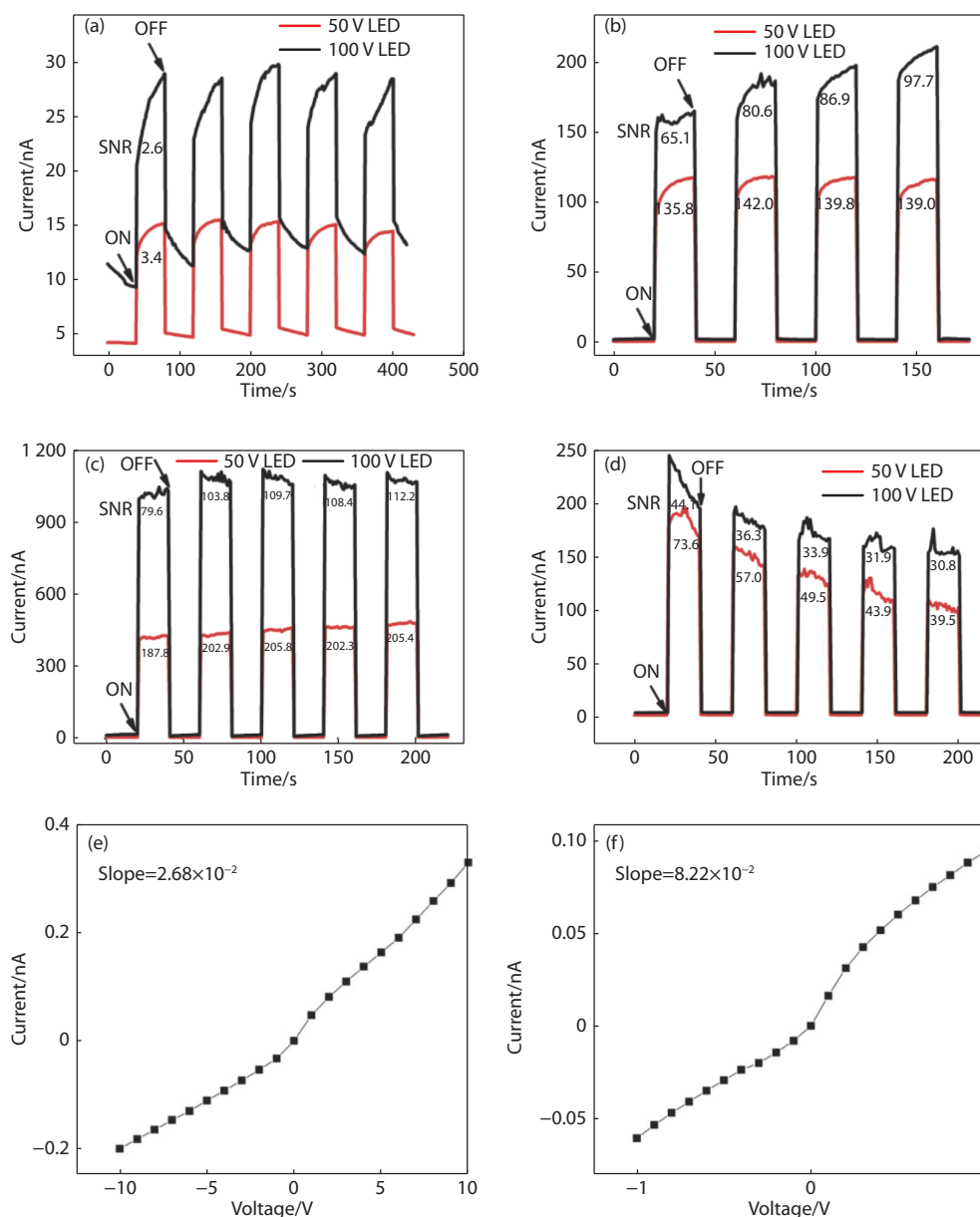


Fig. 8 Photoresponse results of CsPbBr₃ detectors from different samples with Ag/Ag contact. (a) sample 1100. (b) sample 1127. (c) sample 1149. (d) sample 1153. Current-voltage (I-V) curves of (e) sample 1127 from -10 to 10 V, (f) sample 1149 from -1 to 1 V.

Table 3. Pb/Cs molar ratios of 4 samples after crystal growth.

Sample	Starting Materials		After Crystal Growth	
	PbBr ₂ /CsBr		Pb	Cs
1100	1.00: 1.00		1.0139 ± 0.006	1.0000 ± 0.006
1127	1.00: 1.00		1.0115 ± 0.008	1.0000 ± 0.005
1149	1.02: 1.00		1.0117 ± 0.008	1.0000 ± 0.005
1153	1.00: 1.01		1.0117 ± 0.005	1.0000 ± 0.003

does not affect the internal Pb/Cs molar ratio in as-grown single crystals. However, samples with different ratios of precursors did display a significantly different photoresponse performance.

In comparison to sample 1127, the photosensitivity was significantly enhanced in sample 1149 (Fig. 8c), which started with a 2% molar extra PbBr₂ during synthesis. The SNR

reached over 200 at 50 V and over 100 at 100 V, presenting the best photoresponse among the tested samples. However, due to the surface discharge and contact issues, electrical current fluctuations were observed for the devices under a 100V bias. The nature of this instability is under investigation. Sample 1153 (Fig. 8d), which started with 1% molar ratio extra CsBr, shared a similar dark current at around 2 nA at 50 V as sample 1149, but exhibit a much lower photo current. The improvement of photo-responses with increasing PbBr₂ to CsBr ratio in the starting materials suggested that the excess of Pb prohibits the formation of certain charge carrier trapping defects, while the overall chemical stoichiometry of the CsPbBr₃ systems is not affected.

The intrinsic resistivity measurements of different samples in the dark conditions have also been investigated *via* characteristic current-voltage (I-V) curves. Fig. 8e and 8f show the I-V

curves measured for sample 1127 and 1149, respectively. All samples reached a resistivity at around $10^8\sim 10^9 \Omega\cdot\text{cm}$, meeting the requirements of high resistivity for high-performance radiation detector materials.

3.6 Pulse-height spectrum of CsPbBr₃ semiconductor

The pulse-height spectra a $0.9\mu\text{Ci } ^{241}\text{Am}$ source were collected using a CsPbBr₃ detector device produced from sample 1149, as shown in Fig. 9. With increasing applied negative voltages, higher energy signals were detected, indicating that the device exhibited a good spectral response towards the radiation source. However, further improvement on grown crystals and device configurations are necessary to improve the charge collection and energy resolution. A pulse captured on an oscilloscope connected to the output of the preamplifier is shown in Appendix C.

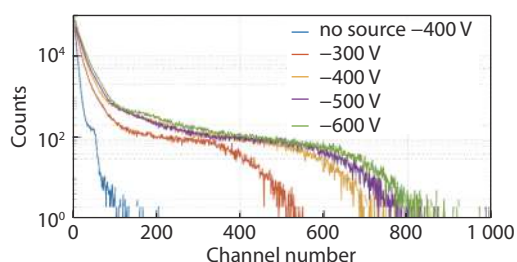


Fig. 9 Pulse-height spectrum collected for the CsPbBr₃ crystal device with a Ga\CsPbBr₃\Ga configuration.

4 Conclusions

High-quality CsPbBr₃ single crystals were successfully grown via a modified zone refining process. High purity crystals were obtained with a total impurity level of less than 1 ppm. In the grown single crystals, WDS analyses revealed a slight deviation from the nominal stoichiometry, which is not impacted by the Pb/Cs molar ratio in the starting materials under the zone refining conditions. Photo-electrical measurements of all the samples were carried out. The obtained CsPbBr₃ semiconductor detectors reached a high resistivity within a range of $10^8\sim 10^9 \Omega\cdot\text{cm}$. Compared to the non-zone refining sample, photo-responses of the zone refined CsPbBr₃ detector devices are improved by a factor of tens. Among all the other zone-refined samples, the sample started with a 2% molar ratio of extra PbBr₂ during the synthesis exhibited the best photo-response performance, indicating the Pb rich condition prohibits the formation of certain charge carrier trapping defects. The pulse-height spectrum of the CsPbBr₃ semiconductor was collected, which exhibited a charge collection response towards the radiation source. Better energy resolution can be achieved by further improvement on the quality of grown crystals and device configurations.

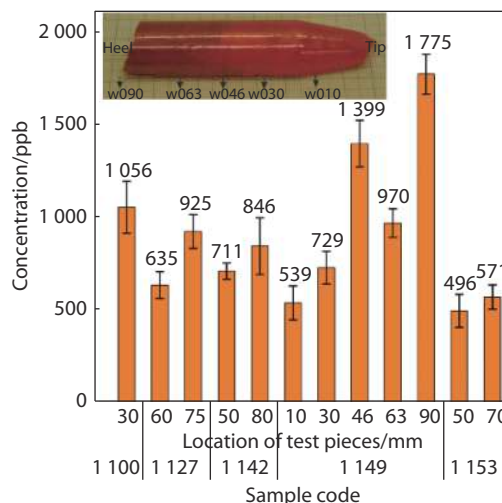
Acknowledgments

The authors acknowledge the Natural Sciences and Engineering Research Council of Canada (NSERC) and the Canada Foundation for Innovation (CFI) for financial support. The authors also acknowledge the support from Arthur B. McDon-

ald Canadian Astroparticle Physics Research Institute and the government of Ontario.

Appendix

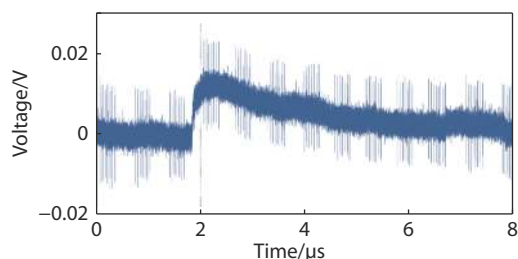
Appendix A. Total impurity concentrations of different samples.



Appendix B. The concentrations of 66 trace elements detected in the sample 1149 w030 by ICP-MS. The total impurity level is around 729 ppb wt.

Elemen	Concentrations	Elemen	Concentrations	Elemen	Concentrations
ts	/ppb wt.	ts	/ppb wt.	ts	/ppb wt.
Li	<MQL	Ge	<MQL	Sm	0.000
Be	<MQL	As	<MQL	Eu	0.013
B	<MQL	Se	1.9	Gd	0.014
Na	465.0	Rb	<MQL	Tb	<MQL
Mg	<MQL	Sr	<MQL	Dy	0.003
Al	<MQL	Y	<MQL	Ho	0.003
Si	<MQL	Zr	<MQL	Er	0.000
P	<MQL	Nb	<MQL	Tm	0.000
S	<MQL	Mo	6.7	Yb	0.002
K	<MQL	Ru	<MQL	Lu	0.000
Ca	<MQL	Rh	246.0	Hf	<MQL
Sc	<MQL	Pd	<MQL	Ta	<MQL
Ti	<MQL	Ag	<MQL	W	<MQL
V	<MQL	Cd	0.000	Re	0.003
Cr	<MQL	Sn	<MQL	Os	<MQL
Mn	<MQL	Sb	<MQL	Ir	<MQL
Fe	<MQL	Te	<MQL	Pt	<MQL
Co	<MQL	Ba	0.539	Au	<MQL
Ni	<MQL	La	0.038	Tl	0.926
Cu	<MQL	Ce	0.061	Bi	8.5
Zn	<MQL	Pr	0.001	Th	<MQL
Ga	<MQL	Nd	<MQL	U	<MQL

Appendix C. A pulse was captured on an oscilloscope connected to the output of the preamplifier.



Conflict of interest

The authors declare no conflict of interest.

Author contributions

Trace impurity analysis of CsPbBr₃ crystals by ICP-MS was conducted by Alexandre Voinot in the Department of Geological Sciences and Geological Engineering at Queen's University.

Elemental analysis of CsPbBr₃ crystals by WDS was performed by Brian Joy and Steve Beyer in the Department of Geological Sciences and Geological Engineering at Queen's University.

Matthew Webster, from the Department of Physics, Engineering Physics & Astronomy at Queen's University, constructed the instrument used for photosensitivity measurements and carried out pulse-height measurement and analysis.

Apart from the above experiments, the research work presented in this manuscript was performed by Yu Wu under the supervision of Prof. Peng Li Wang in the Department of Chemistry at Queen's University.

REFERENCES

1. T. E. Schlesinger, J. E. Toney, H. Yoon, E. Y. Lee, B. A. Brunett, L. Franks, R. B. James, *Materials Science and Engineering: R: Reports*, 2001, 32, 103
2. S. D. Sordo, L. Abbene, E. Caroli, A. M. Mancini, A. Zappettini, P. Ubertini, *Sensors*, 2009, 9, 3491
3. H. H. Barrett, J. D. Eskin, H. B. Barber, *Physical Review Letters*, 1995, 75, 156
4. P. M. Johns, J. C. Nino, *Journal of Applied Physics*, 2019, 126, 040902
5. A. Mirzaei, J.-S. Huh, S. S. Kim, H. W. Kim, *Electronic Materials Letters*, 2018, 14, 261
6. L. Gao, Q. Yan, *Solar RRL*, 2020, 4, 1900210
7. B. D. Milbrath, A. J. Peurrung, M. Bliss, W. J. Weber, *Journal of Materials Research*, 2008, 23, 2561
8. K. Hitomi, T. Tada, S. Kim, Y. Wu, T. Tanaka, T. Shoji, H. Yamazaki, K. Ishii, *IEEE Trans. Nucl. Sci.*, 2011, 58, 1987
9. C. Szeles, *IEEE Trans. Nucl. Sci.*, 2004, 51, 1242
10. W. Lin, Z. Liu, C. C. Stoumpos, S. Das, Y. He, I. Hadar, J. A. Peters, K. M. McCall, Y. Xu, D. Y. Chung, B. W. Wessels, M. G. Kanatzidis, *Crystal Growth & Design*, 2019, 19, 4738
11. U. N. Roy, G. S. Camarda, Y. Cui, R. Gul, A. Hossain, G. Yang, J. Zazvorka, V. Dedic, J. Franc, R. B. James, *Scientific Reports*, 2019, 9, 1620
12. K. Hitomi, T. Shoji, K. Ishii, *Journal of Crystal Growth*, 2013, 379, 93
13. G. F. Knoll, *Radiation Detection and Measurement*, John Wiley & Sons, America, 2010.
14. M. Ahmadi, T. Wu, B. Hu, *Advanced Materials*, 2017, 29, 1605242

15. X. Li, Y. C. Wang, L. Zhu, W. Zhang, H. Q. Wang, J. Fang, *ACS Appl. Mater. Interfaces*, 2017, 9, 31357
16. Z. Chen, Q. Dong, Y. Liu, C. Bao, Y. Fang, Y. Lin, S. Tang, Q. Wang, X. Xiao, Y. Bai, Y. Deng, J. Huang, *Nat. Commun.*, 2017, 8, 1890
17. B. Han, B. Cai, Q. Shan, J. Song, J. Li, F. Zhang, J. Chen, T. Fang, Q. Ji, X. Xu, H. Zeng, *Advanced Functional Materials*, 2018, 28, 1804285
18. H. Wei, J. Huang, *Nature Communications*, 2019, 10, 1066
19. S. Yakunin, D. N. Dirin, Y. Shynkarenko, V. Morad, I. Cherniukh, O. Nazarenko, D. Kreil, T. Nauser, M. V. Kovalenko, *Nature Photonics*, 2016, 10, 585
20. J. Yu, G. Liu, C. Chen, Y. Li, M. Xu, T. Wang, G. Zhao, L. Zhang, *Journal of Materials Chemistry C*, 2020, 8, 6326
21. B. Conings, J. Drijkoningen, N. Gauquelin, A. Babayigit, J. D'Haen, L. D'Olieslaeger, A. Ethirajan, J. Verbeeck, J. Manca, E. Mosconi, F. D. Angelis, H.-G. Boyen, *Advanced Energy Materials*, 2015, 5, 1500477
22. G. P. Nagabhushana, R. Shivaramaiah, A. Navrotsky, *Proceedings of the National Academy of Sciences*, 2016, 113, 7717
23. C. C. Stoumpos, C. D. Malliakas, J. A. Peters, Z. Liu, M. Sebastian, J. Im, T. C. Chasapis, A. C. Wibowo, D. Y. Chung, A. J. Freeman, B. W. Wessels, M. G. Kanatzidis, *Crystal Growth & Design*, 2013, 13, 2722
24. Y. He, L. Matei, H. J. Jung, K. M. McCall, M. Chen, C. C. Stoumpos, Z. Liu, J. A. Peters, D. Y. Chung, B. W. Wessels, M. R. Wasielewski, V. P. Dravid, A. Burger, M. G. Kanatzidis, *Nature Communications*, 2018, 9, 1609
25. J. Kang, L.-W. Wang, *The Journal of Physical Chemistry Letters*, 2017, 8, 489
26. J. Ding, S. Du, Z. Zuo, Y. Zhao, H. Cui, X. Zhan, *The Journal of Physical Chemistry C*, 2017, 121, 4917
27. B. Murali, H. K. Kolli, J. Yin, R. Ketavath, O. M. Bakr, O. F. Mohammed, *ACS Materials Letters*, 2020, 2, 184
28. X. Cheng, S. Yang, B. Cao, X. Tao, Z. Chen, *Advanced Functional Materials*, 2020, 30, 1905021
29. D. Y. Chung, M. G. Kanatzidis, F. Meng, C. D. Malliakas, SPIE Optics + Photonics, San Diego, CA, USA, August 2016.
30. M. Zhang, Z. Zheng, Q. Fu, Z. Chen, J. He, S. Zhang, C. Chen, W. Luo, *Journal of Crystal Growth*, 2018, 484, 37
31. K. Wang, L. Jing, Q. Yao, J. Zhang, X. Cheng, Y. Yuan, C. Shang, J. Ding, T. Zhou, H. Sun, W. Zhang, H. Li, *The Journal of Physical Chemistry Letters*, 2021, 12, 1904
32. J.-L. Pouchou, F. Pichoir, *Electron Probe Quantitation*, Springer, Germany, 1991.
33. K. F. J. Heinrich, 11th Int. Congr. on X-Ray Optics and Microanalysis, London, Ontario, Canada, August 1986.
34. K. L. Williams, *An introduction to X-ray spectrometry: X-ray fluorescence and electron microprobe analysis*, Allen & Unwin Boston, America, 1987.
35. H. Zhang, F. Wang, Y. Lu, Q. Sun, Y. Xu, B.-B. Zhang, W. Jie, M. G. Kanatzidis, *Journal of Materials Chemistry C*, 2020, 8, 1248
36. H. Kim, Y. Ogorodnik, A. Kargar, L. Cirignano, C. L. Thrall, W. Koehler, S. P. O'Neal, Z. He, E. Swanberg, S. A. Payne, M. R. Squillante, K. Shah, *Frontiers in Physics*, 2020, 8, 55
37. A. Churilov, W. Higgins, G. Ciampi, H. Kim, L. Cirignano, F. Olschner, K. Shah, SPIE Optics+Photonics 2008, San Diego, CA, USA, August 2008.
38. U. Makanda, A. Voinot, R. Kandel, Y. Wu, M. Leybourne, P. Wang, *Journal of Analytical Atomic Spectrometry*, 2020, 35, 2672



©2022 The Authors. *Materials Lab* is published by Lab Academic Press. This is an open access article under the terms of the Creative Commons Attribution License, which permits use, distribution and reproduction in any medium, provided the original work is properly cited.